ACSNANO
www.acsnano.org
ARTICLE

Bioengineered Magnetoferritin Nanoprobes for Single-Dose Nuclear-Magnetic Resonance Tumor Imaging

Yanzhao Zhao,[†,#] Minmin Liang,[‡,#] Xiao Li,[†] Kelong Fan,[‡] Jie Xiao,[†] Yanli Li,[†] Hongcheng Shi,[†] Fei Wang,[‡] Hak Soo Choi,[*,§] Dengfeng Cheng,[*,†] and Xiyun Yan[*,‡]

[†]Department of Nuclear Medicine, Zhongshan Hospital, Fudan University/Shanghai Institute of Medical Imaging, Shanghai 200032, China

[‡]Key Laboratory of Protein and Peptide Pharmaceutical/Chinese Academy of Sciences-University of Tokyo Joint Laboratory of Structural Virology and Immunology/Beijing Translational Engineering Center of Biomacromolecular Drugs, Institute of Biophysics, Chinese Academy of Sciences, Beijing 100101, China

[§]Division of Hematology/Oncology, Department of Medicine, Beth Israel Deaconess Medical Center and Harvard Medical School, Boston, Massachusetts 02215, United States

Supporting Information

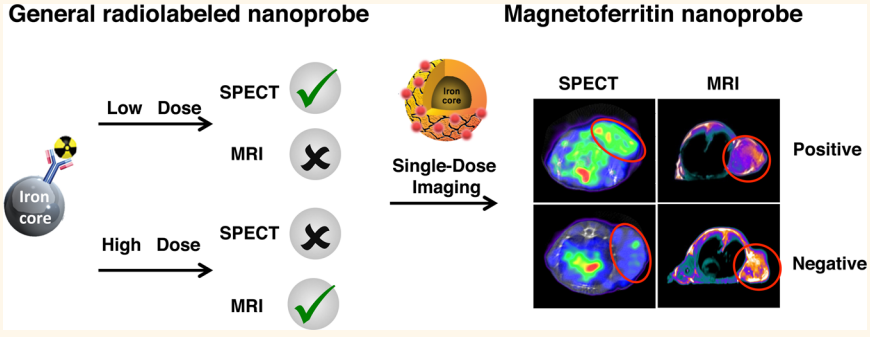

ABSTRACT: **Despite all the advances in multimodal imaging, it remains a significant challenge to acquire both magnetic resonance and nuclear imaging in a single dose because of the enormous difference in sensitivity. Indeed, nuclear imaging is almost 10^6-fold more sensitive than magnetic resonance imaging (MRI); thus, repeated injections are generally required to obtain sufficient MR signals after nuclear imaging. Here, we show that strategically engineered magnetoferritin nanoprobes can image tumors with high sensitivity and specificity using SPECT and MRI in living mice after a single intravenous injection. The magnetoferritin nanoprobes composed of ^{125}I radionuclide-conjugated human H-ferritin iron nanocages (^{125}I-M-HFn) internalize robustly into cancer cells *via* a novel tumor-specific HFn-TfR1 pathway. In particular, the endocytic recycling characteristic of TfR1 transporters solves the nuclear signal blocking issue caused by the high dose nanoprobes injected for MRI, thus enabling simultaneous functional and morphological tumor imaging without reliance on multi-injections.**

KEYWORDS: *multimodal imaging, diagnostic imaging, nuclear signal blocking, tumor targeting, magnetoferritin nanoparticles*

A combination of morphological imaging and nuclear medicine techniques has been required for comprehensive understanding and characterization of human cancers.[1] In particular, synergizing magnetic resonance imaging (MRI) with positron emission tomography (PET) or single photon emission tomography (SPECT) offers highly complementary information for tumor characterization *in vivo*. MRI provides high spatial resolution structural images with high soft-tissue contrast but low sensitivity and signal-to-noise ratios,[2] while SPECT and PET imaging modalities show very high sensitivity with relatively low imaging resolution.[3] The combination of SPECT-PET with MRI provides sufficient spatial and temporal resolutions as well as high sensitivity.

Despite the clinical and preclinical availability of hybrid PET/MRI and SPECT/MRI scanners,[4] no imaging agents can serve as dual modality imaging probes in clinical practice[5,6] because nuclear imaging is extremely more sensitive than MRI. For example, MRI would require >10^7 Gd atoms[7] or >10^6 high

Received: November 25, 2015
Accepted: March 4, 2016
Published: March 9, 2016

DOI: 10.1021/acsnano.5b07408
ACS Nano 2016, 10, 4184–4191

relaxivity of iron oxide nanoparticles (NPs)[8] to detect a single cell, whereas SPECT-PET imaging requires around 0.01−0.2 radioatoms per cell.[7] The enormous difference in sensitivity limits the radiolabeling of imaging probes with very low specific activities (radioactivity per unit mass of imaging probe) because of the excess nonradiolabeled cold probes. More importantly, they block the specific binding of the radiolabeled hybrid probes to their tumor targets, resulting in low tumor specificity.[9] Thus, repeated multiple injections are usually required to acquire individual SPECT-PET and MR imaging, even with the advanced SPECT-PET/MRI integrated scanners. However, the repeated injection of imaging probes is not desired in clinical practice because of increased unpredictable risks with high-accumulated dosage during long-term treatments.[10]

Ferritin is a self-assembled spherical iron storage protein composed of 24 subunits of two types, heavy-chain ferritin (HFn) and light-chain ferritin (LFn).[11,12] The interior cavity of ferritin is a useful template to synthesize highly crystalline and monodispersed nanoparticles (NPs).[13−15] In 2010, Li and colleagues reported that HFn binds to human cells *via* transferrin receptor 1 (TfR1).[16] Although it is well-known that TfR1 is overexpressed on most malignant cells and has long been studied well as a tumor biomarker, current HFn-based tumor diagnosis and therapy still rely on the surface functionalization using targeting ligands to achieve specific tumor uptake.[17−21] We recently reported that human HFn selectively accumulates into tumors *in vivo* by TfR1-mediated specific targeting followed by rapid internalization without necessitating extra targeting ligands.[22,23]

By utilizing the intrinsic tumor-targeting property and unique nanocage structure of human HFn, we herein synthesized a highly crystalline iron oxide NP within the interior cavity of HFn and radiolabeled the outer surface for tumor SPECT/MR imaging. Because TfR1 constitutively recycles between the cell surface and intracellular compartments independently of ligand binding,[24,25] HFn can therefore deliver high concentration of SPECT/MRI hybrid imaging probes into tumors and achieve dual-modality imaging *via* the unique HFn-TfR1 pathway.[25,26] In particular, the independent recycling characteristic of TfR1 transporter make it not easily be blocked by the non-radiolabeled cold probes during nuclear imaging, making it possible to image tumors using both SPECT and MRI.

Although several SPECT-PET/MRI contrast agents have been reported based on the combination of radioisotopes with superparamagnetic iron oxide NPs, the majority achieved bimodal tumor imaging relying on multi-injection.[26−30] A few used a mixture of imaging agents from each modality making tumor imaging bimodal (e.g., injection of ^{18}F-FDG to obtain tumor PET imaging, and at the same time, use an MRI contrast agent such as Gd-DTPA for MR image acquisition).[31] There are also some contrast agents that achieved single-dose multimodal imaging for reticuloendothelial and lymphatic systems by subcutaneously injecting radiolabeled iron oxide NPs.[32−34] These nanoprobes passively accumulated in reticuloendothelial and lymphatic systems through macrophages to achieve simultaneous target bimodal imaging, which avoids the typical nuclear signal blocking issue caused by the receptor-mediated active tumor targeting. Only two small studies demonstrated single-dose PET-MRI tumor detection by intratumoral injection of ^{124}I labeled $Gd_3N@C_{80}$ nanoparobes[35] or by employing dendrimer-chelated Gd^{3+} and ^{68}Ga.[36] No study has prospectively addressed a mechanism or a nanoprobe which can break through the obvious sensitivity limitation between MRI and PET/SPECT to achieve single-dose MRI/nuclear tumor-targeted imaging. This study represents the first demonstration of a hybrid imaging nanoprobe that solved the excess nonradiolabeled probe blocking issue during nuclear imaging because of the enormous difference in sensitivity and achieved highly contrast-enhanced SPECT/MRI tumor imaging in a single-dose injection.

RESULTS

Development and Characterization of ^{125}I-M-HFn NPs. Recombinant human HFn was expressed and purified from *E. coli*, as described previously.[22,23] Magnetoferritin (M-HFn) NPs were prepared by loading Fe^{2+} into the cavities of HFn nanocages through the iron ion channel on the surface of HFn, followed by the formation of an iron oxide nanocore within the HFn nanocage by oxidation in the presence of H_2O_2. We further radiolabeled the surface of the NPs with ^{125}I using Iodogen, resulting in M-HFn NPs with an ^{125}I radiotracer (i.e., ^{125}I-M-HFn NPs; Figure 1A). After purification, the physicochemical properties of ^{125}I-M-HFn NPs were extensively characterized (Figure 1 and Supporting Information, Figures S1−S4). Cryo-electron microscopy (cryo-EM) analysis confirmed the uniformly spherical and monodispersed iron cores with an average diameter of 4.8 nm that were clearly encapsulated within the HFn protein nanocage (Figure 1B). The average number of iron ions within the nanocage was determined to be 2210 ± 230 (mean ± SD) per particle by inductively coupled plasma atomic emission spectroscopy (ICP-AES). The MR contrast properties of M-HFn NPs were next evaluated *in vitro* using 2% agarose phantoms.

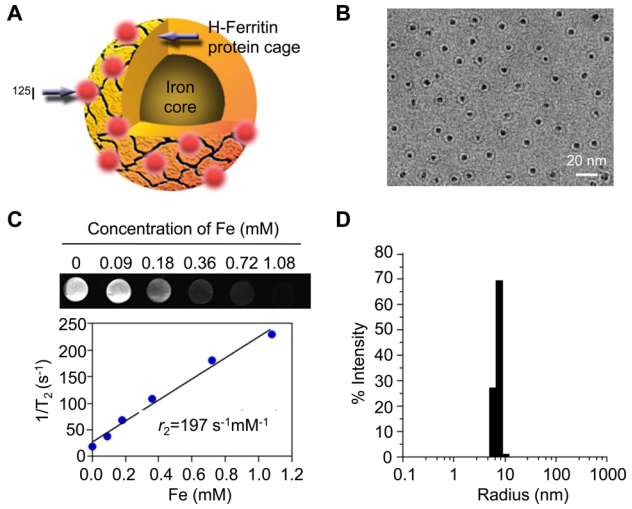

Figure 1. Preparation and characterization of ^{125}I-M-HFn NPs: (A) schematic illustration of the ^{125}I-M-HFn NPs; (B) cryo-EM images of the monodispersed spherical particles; (C) T2-weighted MR images of ^{125}I-M-HFn NPs at different concentrations and their T2 relaxation time plot (bottom); (D) hydrodynamic diameter of ^{125}I-M-HFn NPs determined by DLS.

The longitudinal (T1) and transverse (T2) relaxation times were measured at 3.0-T magnetic field based on the iron concentration of M-HFn, and the relaxivities were determined to be r_1 = 15.0 mM^{-1} s^{-1} (Figure S1) and r_2 = 197 mM^{-1} s^{-1} (Figure 1C). M-HFn showed 2−3 fold higher relaxivity than the commercial Feridex and Ferucarbotran, of which relaxivity

DOI: 10.1021/acsnano.5b07408
ACS Nano 2016, 10, 4184−4191

was 93 and 57 mM^{-1} s^{-1} (3.0-T), respectively.[37] The high r_2 value is likely due to the strong perturbation effect of the outside HFn nanocage on the nearby water molecules around the iron core.[38] In addition, the multiple magnetite nanocrystal cores of M-HFn NPs also contributed to their high MR contrast effect.[39] The natural iron cores in holoferritin, mainly consisting of the hydrated iron oxide mineral ferrihydrite ($5Fe_2O_3{\cdot}9H_2O$),[40] exhibited a low r_2 relaxivity (28.5 mM^{-1} s^{-1}) (Figure S2). Nevertheless, the high contrast property of M-HFn NPs highlights its potential as an *in vivo* imaging probe.

The following dynamic light scattering (DLS) measurements further demonstrated that the resulting particles were monodispersed with an outer hydrodynamic diameter of ~14 nm (Figure 1D). CD spectra results verified that either iron loading or radiolabeling did not significantly perturb the overall protein cage architecture of HFn (Figure S3). We have also measured the serum stability of ^{125}I-M-HFn NPs by monitoring ^{125}I release and HFn protein degradation over the course of incubation in fetal bovine serum. A radiochemical purity of >80% was detected after 12 h of incubation at 37 °C (Figure S4), indicating that ^{125}I-M-HFn NPs are stable enough in the circulation *in vivo* to allow sufficient time for their uptake into tumors.

High Uptake of ^{125}I-M-HFn NPs in Tumor Cells. We have previously demonstrated that human HFn specifically binds to human cancer cells and accumulates into the tumor *via* TfR1-mediated specific targeting and the subsequent robust internalization.[23] The HFn nanocarrier should therefore be able to deliver high concentrations of imaging probes into tumor cells. We next investigated tumor-specific uptake of ^{125}I-M-HFn NPs in TfR1-positive and TfR1-negtive tumor cells. HT-29 human colon cancer cells express TfR1 at high levels, but MX-1 human breast cancer cells do not express this receptor (Figure 2A). We incubated HT-29 and MX-1 cells with 20 μCi of ^{125}I-M-HFn for 1 h with constant motion. After the incubated cells were washed with PBS, their radioactivity was determined with the use of a gamma counter and measured the iron uptake within the cells using ICP-AES. SPECT and T2-weighted MRI images were subsequently acquired. Figure 2B shows that ^{125}I-M-HFn NPs are 7.8-fold more specific to TfR1-positive HT-29 cancer cells compared to TfR1-negative MX-1 cells, indicating TfR1-mediated specific binding of ^{125}I-M-HFn to cancer cells. After 1 h of incubation, HT-29 simultaneously internalized ~670 nCi of radioactivity and ~1.6 μg of iron per 10^6 cells (Figure 2C), which can be easily detected by both SPECT and MRI (Figure 2B). To the best of our knowledge, this represents the first demonstration of a targeting nanocarrier that can simultaneously deliver such high doses of nuclear and MR imaging probes into tumor cells.

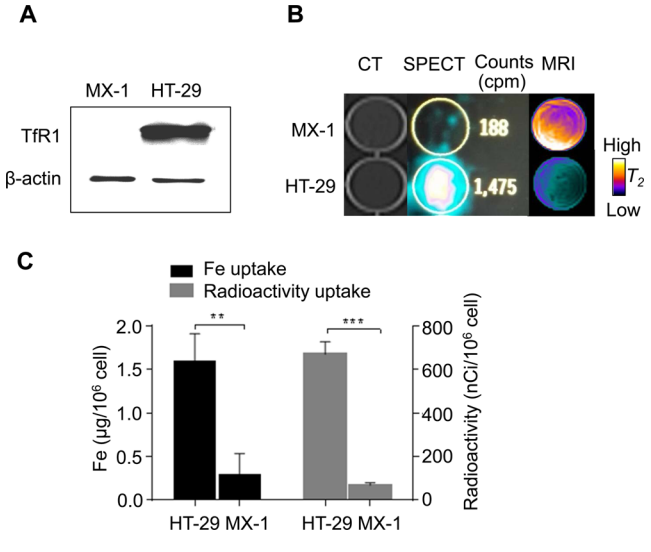

Figure 2. *In vitro* MRI and SPECT detection of NP-labeled tumor cells. (A) Western blot of TfR1 expression in MX-1 and HT-29 cancer cells. β-actin was used as a loading control. (B) T2-weighted MRI and SPECT imaging of ^{125}I-M-HFn NPs after incubation with MX-1 and HT-29 cancer cells. (C) Cellular uptake of ^{125}I-M-HFn NPs measured by ICP-AES and gamma counter, respectively (n = 5, mean ± SD, unpaired Student's t-test, $^{**}P < 0.01$, $^{***}P < 0.001$).

TfR1 is often overexpressed in various tumor cells and has long been used as a targeting marker for cancer theranostics. We then evaluated the universality of ^{125}I-M-HFn for recognizing cancer cells.^{125}I-M-HFn shows significant binding to 15 types of cancer cells, including A375 melanoma cells, MDA-MB-231 and MCF-7 breast cancer cells, U87-MG glioblastoma cells, K562 erythroleukemia cells, HeLa cervical cancer cells, SMMC-7721 and HepG-2 hepatocellular carcinoma cells, SKOV-3 ovarian cancer cells, PC-3 prostate cancer cells, U251 glioblastoma cells, U937 histiocytic lymphoma cells, SW1990 pancreatic cancer cells, and Jurkat T-cell leukemia cells (Supporting Information, Table S1), demonstrating the ability of ^{125}I-M-HFn NPs to universally recognize cancer cells.

***In Vivo* SPECT/MRI Tumor Imaging Using ^{125}I-M-HFn NPs.** We next evaluated the performance of ^{125}I-M-HFn NPs for tumor dual-modality imaging in mice bearing HT-29 or MX-1 xenografts. A single-dose of ^{125}I-M-HFn NPs containing 500 μCi (^{125}I) and 11.2 μg (Fe) in 100 μL of PBS was injected into tumor-bearing mice through the tail vein. SPECT and MR imaging were performed consecutively on each mouse before and after 2 h and 6 h intravenous injection of ^{125}I-M-HFn NPs, respectively. The SPECT images demonstrated high ^{125}I-M-HFn uptake in the TfR1-positive HT-29 tumor with a positive-to-negative tumor ratio of 2.8 ± 0.21 and 2.6 ± 0.27 over 2 h and 6 h postinjection, respectively (Figure 3A). The further SPECT quantitative analysis provides accurate quantitative assessment of ^{125}I-M-HFn uptake in tumor (Figure 3C). Pre- and post-contrast-enhanced T2-weighted MR images reveal the complementary morphological information (Figure 3B). MRI at 6 h postinjection was in good correspondence to nuclear imaging with significant signal intensity decrease (78 ± 14%) in HT-29 tumor area as compared to preinjection. In contrast, we observed a slight uptake of the SPECT radiotracers and less than 30% decrease of signal intensity at TfR1-negtive MX-1 tumor areas (Figure 3A–C). The high HT-29 tumor radioactivity uptake obscured the slight absorbance of MX-1 tumors and affected the MX-1 tumor signals to be relatively weak when the same scale was used for the SPECT images (Figure 3A). The following Prussian blue staining further confirmed the presence of ^{125}I-M-HFn in TfR1-positive HT-29 tumors, but little in TfR1-negative MX-1 tumors (Figure S5). Thus, with only a single-dose injection, ^{125}I-M-HFn NPs could achieve tumor *in vivo* imaging with both SPECT and MRI.

We followed the pharmacokinetics and biodistribution of ^{125}I-M-HFn NPs in tumor-bearing mice. The elimination blood half-life ($t_{1/2\beta}$) was found to be of 204.3 min (Figure S6), and the background signals in major healthy tissues/organs decreased over the period of observation (Table S2), indicating rapid clearance of ^{125}I-M-HFn from the whole body and minimal radiation exposure to healthy organs. The tumor-to-

DOI: 10.1021/acsnano.5b07408
ACS Nano 2016, 10, 4184–4191

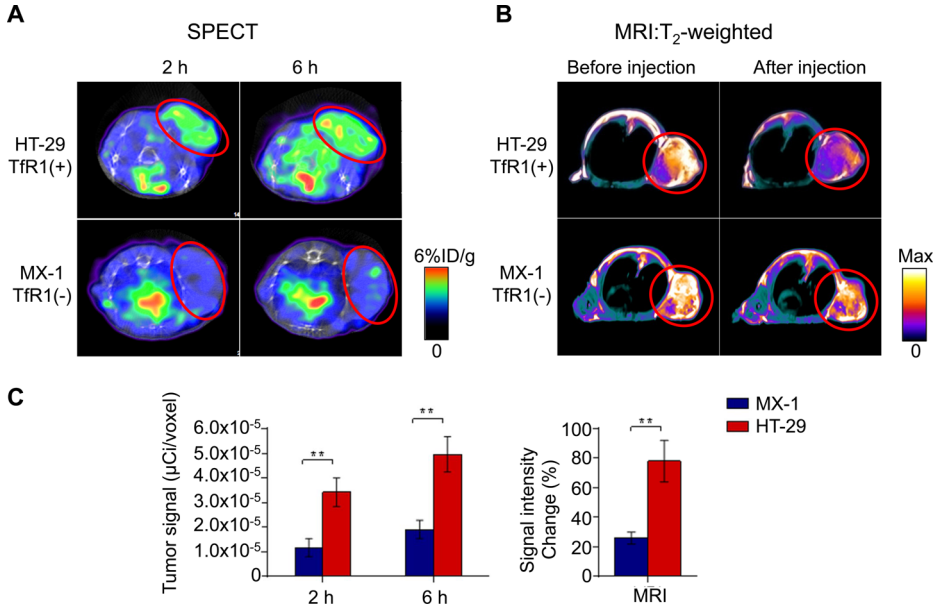

Figure 3. *In vivo* SPECT-MRI tumor imaging in living mice using ^{125}I-M-HFn NPs. Tumor images (red circles) were obtained using (A) SPECT at 2 h and 6 h postinjection and (B) T2-weighted MRI at 6 h postinjection. (C) Quantitative analysis of TfR1(+) and TfR1(−) tumor images obtained from SPECT and MRI images (n = 5, mean ± SD, unpaired Student's t-test, $^{**}P < 0.01$).

background ratio against muscle and intestines was 9.3 and 21.0 at 24 h postinjection, respectively (Table S2), suggesting that clear HT-29 colon tumor imaging can be obtained within 24 h postinjection. However, 24 h postinjection was not a good time-point for MRI tumor imaging because of the low probe concentration in the tumor (0.84% ID/g, Table S2) and the low sensitivity of MRI. Therefore, to achieve highly contrast-enhanced tumor imaging by both SPECT and MRI, animals were scanned 6 h postinjection. In addition, the 6 h imaging time-point is also convenient for future clinical applications.

We further investigated the mechanism by which ^{125}I-M-HFn NPs achieve tumor SPECT/MR imaging *via* HFn-TfR1 targeting pathway. We labeled M-HFn NPs with FITC and incubated them with HT-29 tumor cells for fluorescence microscopy observation. Cells were simultaneously stained with Cy5.5-labeled transferrin for TfR1 tracking. The fluorescence incubation solution was washed off before warming the cells up from 0 to 37 °C to allow M-HFn endocytosis. As shown in Figure 4, simultaneous binding and uptake of transferrin and HFn were observed (Figure 4, top two panels), confirming the endocytosis of M-HFn NPs *via* TfR1. After delivering M-HFn NPs into the tumor cells, TfR1 recycled back to the cell surface for another delivery as evident by the relocalization of TfR1 on the cell surface (Figure 4, bottom left panel), which explains why HFn-TfR1 targeting strategy can deliver high concentrations of imaging probes into tumor cells.

We next performed experiments to show that the excess dose of nonradiolabeled imaging probes do not block HFn-TfR1 targeting strategy. We intravenously injected 500 μCi of ^{125}I-M-HFn NPs with or without coinjection of 50-fold excess nonradiolabeled cold M-HFn into HT-29 tumor-bearing mice and scanned the mice after 6 h in a NanoSPECT/CT system. Figure 5A shows that the mice that received an excess dose of cold M-HFn coinjection produced no decrease in tumor radioactivity uptake compared to a single-dose of ^{125}I-M-HFn NPs-injected mice. Instead, the tumor radioactivity significantly increased by 54%, from 2.51 ± 0.24%ID/g to 3.86 ± 0.54%ID/g (P = 0.0011, unpaired Student's t-test) after an excess dose of

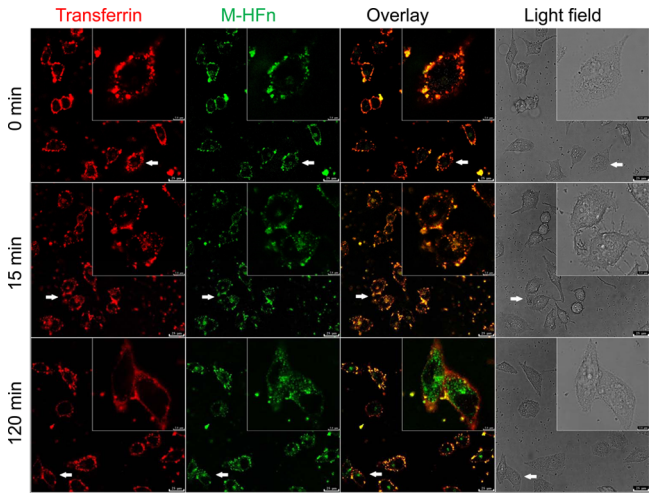

Figure 4. M-HFn NPs are internalized into tumor cells through HFn-TfR1 targeting pathway. HT-29 cells were simultaneous stained with the M-HFn-FITC and holo-transferrin-Cy5.5 for the times indicated to show the endocytic process of M-HFn NPs and the recycling of TfR1. Cells incubated for 30 min on ice were defined as the time point of zero. After washing, cells were warmed up to 37 °C for 15 or 120 min to allow the internalization of M-HFn and the endocytic recycling of TfR1. Arrows indicate the magnified areas shown in the upper right corner of each panel. Scale bars = 25 or 7.5 μm in magnified images.

cold M-HFn, which was further confirmed by the biodistribution data (Figure 5B). We presumed that this effect might have resulted from the prolonged plasma half-life of ^{125}I-M-HFn, as evident by the significantly increased blood concentration of ^{125}I-M-HFn (Figure 5B), which facilitated the time-dependent accumulation of ^{125}I-M-HFn NPs in the tumor. The increased radioactivity uptake in organs was also due to the substantially higher blood concentration when excess cold M-HFn was coadministrated. This result demonstrates that HFn vehicles can deliver high radiation dosage of

DOI: 10.1021/acsnano.5b07408
ACS Nano 2016, 10, 4184–4191

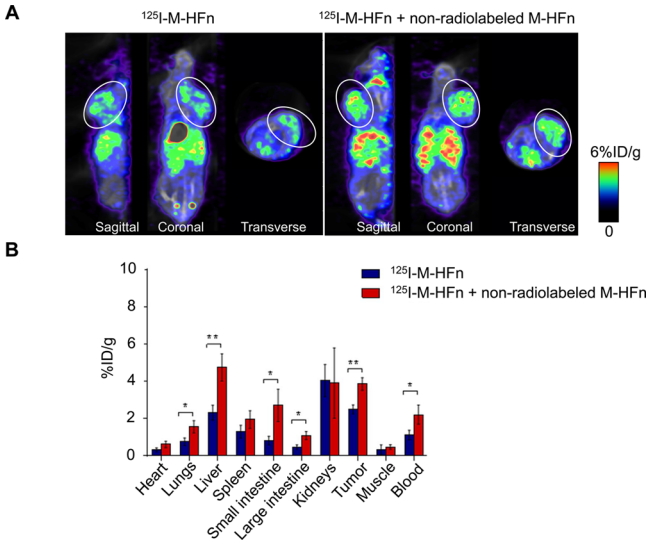

Figure 5. An excess dose of nonradiolabeled M-HFn does not block the radioactivity uptake in tumor *in vivo*. (A) SPECT images of ^{125}I-M-HFn NPs in HT-29 tumor-bearing mice with (left) and without (right) coinjection of 50-fold excess dose of nonradiolabeled M-HFn. White circles indicate tumors. The maximum color values on the two panels are identical. (B) Biodistribution of ^{125}I-M-HFn NPs with and without coinjection of nonradiolabeled M-HFn NPs. Data are expressed as %ID/g ± SD (n = 5, mean ± SD, unpaired Student's t-test, *P < 0.05, **P < 0.01).

^{125}I-M-HFn into tumors even in the presence of excess cold M-HFn, which explains why HFn can achieve tumor SPECT/MRI imaging with a single-dose injection.

Indeed, the "cold probe blocking issue" is generally caused by the excess injected cold probes (e.g., ≥ 50-fold) that compete with the radiolabeled "hot" probes for binding to the limited receptors on the cells, and thus result in blocking the specific tumor uptake of hot probes. This is also one of the main obstacles for achieving dual modality nuclear/MR imaging *via* a single-dose injection. The improved tumor SPECT/MR imaging could be obtained through the HFn-TfR1-based endocytic recycling pathway, which avoids blocking issue of nuclear probes on the cell surface and provides enough iron concentration for MRI, and thus achieves single-dose tumor SPECT/MR imaging.[41,42]

Given the uptake of the contrast agent in normal tissue, we finally evaluated the binding specificity of HFn between human tumor and normal tissues by staining 60 clinical tumor tissue samples and 60 normal tissue samples using FITC-labeled HFn. Staining was considered positive when 10% or more of the tumor cells were stained (cutoff, 10%). As shown in Figure S7, HFn did not stain, or only slightly stained human normal tissues when compared to strongly stained tumor tissues. Furthermore, HFn also displayed a distinct staining intensity among different cancer grades. The results demonstrate that HFn has an impressive capability to discriminate cancerous cells from normal tissues, and thus the slight uptake of HFn in normal tissues would not disturb the cancer diagnosis of ^{125}I-M-HFn *in vivo*.

DISCUSSION

To find out cancer characteristics after a single intravenous injection of tumor-targeted contrast agents is much sought after in molecular cancer imaging. Therefore, there is a great need to develop multimodality imaging probes that can achieve tumor MR and nuclear imaging at the same time. This study show that our developed HFn-TfR1 pathway serves as a novel tumor targeting strategy that can simultaneously deliver a high concentration of MR and nuclear imaging probes into the target tumor and avoid the excess nonradiolabeled cold probes blocking issue, which is the main challenge for achieving single-dose SPECT/MR imaging. Indeed, the biologically engineered ^{125}I-M-HFn NPs achieved highly contrast-enhanced SPECT/MRI tumor imaging after a single intravenous injection (Figure 3) *via* HFn-TfR1 targeting strategy (Figure 4), and the TfR1 transporters were actively recycling independently of ligand binding,[24,25] thus avoiding nuclear signal blocking (Figure 5). ^{125}I was selected in this nanosystem because it is conveniently available, and having the similar chemical properties and *in vivo* behavior with the commonly clinically applied imaging isotope of ^{123}I and ^{124}I, which can easily replace ^{125}I for the future clinical trials.

Our multimodal imaging probe ^{125}I-M-HFn combined with the novel HFn-TfR1 targeting strategy represents three important points of novelty: (1) Robustness. the unique nanocage architecture of HFn can easily payload a variety of signal species including a wide range of metal ions,[13−16] radioisotopes,[19,43] and small molecule contrast agents.[44−47] By combining the robust HFn-TfR1 tumor-targeting strategy, HFn can play as a universal nanoplatform to achieve real multimodal imaging of tumors in one dosage as TfR1 is universally overexpressed in a wide variety of cancer cells (Table S1) and the slight uptake of HFn in normal tissues is not comparable to cancerous tissues and thus would not disturb its specific binding with tumors *in vivo* (Figure S7). (2) Simplicity. HFn nanocages are efficiently produced in *E. coli* at high yield (>100 mg/L from the bacterial lysate)[22,23] and the payload process of imaging moieties in the nanocage is relatively simple. In particular, HFn nanocages intrinsically bind to tumors without necessitating extra modification with targeting ligands, which enables their reproducible preparation at large scale and facilitates future clinical translation. (3) Biocompatibility. HFn naturally exists in humans and is composed of nontoxic elements that therefore would not activate inflammatory or immunological responses. In addition, HFn does not require any surface functionalization or property modulation with extra exterior ligands that might trigger immune responses against the particles. Nevertheless, systematic future work is still required to investigate the biocompatibility of ^{125}I-M-HFn NPs in various *in vivo* applications.

Although HFn-based tumor imaging has been recently reported, almost all the presently available HFn formulations are modified with recognition ligands (e.g., RGD) to achieve tumor-specific targeting.[17−21] These genetically or chemically incorporated exterior surface modifications undoubtedly ruin the intrinsic tumor-targeting property of natural human HFn and increase its immunogenicity. In addition, genetic incorporation of foreign ligands to HFn can seriously affect the self-assembling process of HFn nanocages during their expression *in E. coli* and thus result in a low yield[48,49] [e.g., the typical yields of RGD-modified HFn described in the literature are less than 1/10 that of free HFn[18]].

CONCLUSIONS

There is a great need to develop contrast agents that can simultaneously achieve tumor nuclear and MR imaging in one

DOI: 10.1021/acsnano.5b07408
ACS Nano 2016, 10, 4184−4191

single dose. In this study, we demonstrate that ^{125}I-M-HFn NPs, combining the unique targeting strategy, enable tumor detection *in vivo* with both MRI and SPECT despite the enormous difference of these two modalities in sensitivity. To the best of our knowledge, this study represents the first demonstration of a hybrid imaging nanoprobe that solved the excess nonradiolabeled probe blocking issue during nuclear imaging and achieved highly contrast-enhanced SPECT/MRI tumor imaging in a single-dose injection and therefore lay the foundation for future clinical trial and immediate transfer to the clinic.

METHODS

Preparation and Characterization of ^{125}I-M-HFn NPs. Human HFn was produced in *Escherichia coli* and purified as previously described.[22,23] M-HFn NPs were synthesized and purified using our previously described method.[22] Iodination of M-HFn was performed using the Iodogen method.[50] Iodogen (1,3,4,6-tetrachloro-3α,6α-diphenylglucoluril) is an oxidizing agent that can efficiently activate iodine for spontaneous incorporation into protein tyrosyl groups. The detailed mechanism for iodination of nanoparticles is as follows: iodide (I^-) is first oxidized by Iodogen to form the iodous ion (I^+), which in turn brings the protein iodination by electrophilic substitution reaction at the phenolic ring of tyrosine. Briefly, 0.8 mCi of Na^{125}I (Shanghai GMS Pharmaceutical Co. Ltd.) was mixed with 100 μg of M-HFn in 100 μL of PBS (0.2 M, pH 7.4) and added to a vial coated with 50 μg of Iodogen (Sigma-Aldrich). After incubation for 15 min at room temperature, the mixture was purified with a PD-10 column (GE Healthcare). The final radiochemical yield of purified ^{125}I-M-HFn was >98%. The labeling yield and radiochemical purity of the products were measured by instant thin-layer chromatography (ITLC) on a radio-thin layer scanner (Bioscan).

TfR1 Expression by Western Blotting Analysis. TfR1 expression in HT-29 and MX-1 cell lines was assessed by Western blotting. Cell lysates of each type were run on a 10% SDS–polyacrylamide gel and transferred to a nitrocellulose membrane blocked with 5% nonfat milk, 0.1% Tween 20 in PBS for 30 min, and then incubated overnight at 4 °C with a 1:2000 dilution of mouse antihuman TfR1 monoclonal antibody (mAbs, BD Bioscience). The TfR1 mAbs was detected using a 1:6000 dilution of goat antimouse IgG conjugated to HRP (Pierce), and developed with ECL substrate (Pierce).

Cellular Uptake Studies. The cellular uptake of ^{125}I-M-HFn NPs was investigated in HT-29 and MX-1 cell lines. In a 96-well plate, 1 × 10^6 of HT-29 or MX-1 cells in five duplications were incubated with 20 μCi of ^{125}I-M-HFn in growth medium at 37 °C, in 5% CO_2. After1 h of incubation, the cells were washed with PBS, detached by trypsin and collected by centrifuge. After this, the radioactivity of the incubated cells was counted using a GC-1200 γ counter (ZONKIA, Hefei, China). The same cell samples were further lysed and digested with 2% HNO_3 for intracellular iron content quantification using an ICP-AES instrument (PerkinElmer Optima 8000). The iron concentration was interpolated from a standard curve of the iron standards.

The above cell lines were next imaged on SPECT/CT and MRI to evaluate the binding reactivity of ^{125}I-M-HFn to cancer cells. Briefly, 1 × 10^6 of HT-29 or MX-1 cells were respectively incubated with 20 μCi of ^{125}I-M-HFn NPs in growth medium for 1 h with continuous vortexing at 37 °C. After washing in PBS, the cells were homogeneously suspended in 0.5 mL of 2% agar gel in a 24-well plate. Planar gamma imaging was performed on a clinical SPECT/CT scanner (Precedence, Philips Healthcare) equipped with a low-energy, high-resolution parallel-hole collimator. MR imaging was performed on a clinical MRI scanner (Siemens 3.0-T) equipped with a microsurface coil using a T2-weighted spin–echo sequence (TR = 4000 ms, TE = 13.8 ms, average 3, FOV = 120 × 120 mm, matrix = 256 × 256, slice thickness = 2 mm).

Fluorescence Microscopy of Endocytosis. M-HFn was labeled with FITC (Sigma), and holo-transferrin (Sigma) was labeled with Cy5.5 (GE Healthcare), respectively, according to the manufacturer's instructions. The cellular internalization of M-HFn *via* TfR1 transporter was studied by confocal laser scanning microscopy. Briefly, HT-29 tumor cells were incubated for 30 min at 37 °C in PBS supplemented with 10 mM Tris-HCl, 10 mM Hepes, 5 mM glucose, and 1 mg/mL BSA at pH 7.4. Cells were then incubated with both M-HFn-FITC (1 μM FITC equivalents) and holo-transferrin-Cy5.5 (1 μM Cy5.5 equiv) on ice for 30 min. After being washed in cold PBS, cells were resuspended in buffer at 37 °C to allow endocytosis. At defined time points, internalization was stopped by adding cold PBS containing 0.02% sodium azide. Cells were then washed with cold PBS, fixed in 4% (wt/vol) cold formaldehyde, and plated on poly-L-lysine-treated coverslips (BD Biosciences). Images were collected by a confocal laser scanning microscope (Olympus). The fluorescent signal of Cy5.5 was collected from 650 to 720 nm, and the FITC fluorescent signal was collected from 499 to 550 nm.

***In Vivo* SPECT and MRI Imaging Studies.** All animal studies were performed with the approval of the Ethical Committee of Zhongshan Hospital, Fudan University. For *in vivo* imaging, female BALB/c nude mice of 6 weeks old were implanted subcutaneously with 1 × 10^7 HT-29 or MX-1 tumor cells in the right upper flank. When the xenograft reached about 1.0 cm in diameter, mice were intravenously administered with a single-dose of ^{125}I-M-HFn NPs containing 45 μg (HFn), 500 μCi (^{125}I), and 11.2 μg (Fe) with or without the presence of 50-fold molar excess of nonradiolabeled M-HFn. Mice were imaged consecutively with a small-animal nano-SPECT/CT system (Bioscan) and a 3.0-T clinical MRI scanner (Siemens) before injection and at 2 h and 6 h postinjection. The MRI scanner was equipped with a microsurface coil using a T2-weighted spin–echo sequence (TR = 2500 ms, TE = 35 ms, average 3, FOV = 60 × 60 mm, matrix = 512 × 512, slice thickness =2 mm). Here, the MRI acquisition parameters are different from those for *in vitro* experiments because the *in vivo* physiological environments have different magnetic properties from the *in vitro* MRI surrounding environments, and thus different sequences are needed to acquire the optimal MRI contrast effect for M-HFn nanoparticles.

The SPECT images are slices from the 3D reconstruction obtained using nanoSPECT/CT (Bioscan). The image segmentation and quantitation analysis was performed using *InVivoScope* 1.40 software (Bioscan). Briefly, the volume of interests (VOIs) was obtained in the form of a cylinder, by first circling the regions of interests (ROIs) from the transverse profile, and then selecting the length of ROIs from the maximum intensity projection. Following the above operation, the values of radioactivity and volume of the VOIs were obtained from the software. The radiotracer uptake (μCi/voxel or ID%/cm^3) was calculated by dividing radioactivity by volume from VOIs.

Biodistribution and Statistical Analyses. Female BALB/c mice bearing HT-29 tumors were administered 20 μCi of ^{125}I-M-HFn with or without coinjection of a 50-fold excess of nonradiolabeled cold M-HFn *via* tail vein. At 6 h postinjection, mice were sacrificed and the samples of tumors and organs (heart, lung, liver, spleen, stomach, small intestine, large intestine, kidney, muscle, and blood) were collected, wet-weighed, and counted for radioactivity using a GC-1200 γ counter. Tissue radioactivity concentrations were expressed as the percentage of injected dose per gram of organ (%ID/g). Values are expressed as mean ± SD (n = 5 per group). Statistical analysis was carried out using the unpaired Student's t-test.

ASSOCIATED CONTENT

Supporting Information

The Supporting Information is available free of charge on the ACS Publications website at DOI: 10.1021/acsnano.5b07408.

Detailed descriptions for the characterization of ^{125}I-M-HFn NPs, stability experiment, tissue staining, and biodistribution studies (PDF)

DOI: 10.1021/acsnano.5b07408
ACS Nano 2016, 10, 4184–4191

AUTHOR INFORMATION

Corresponding Authors

*E-mail: hchoi@bidmc.harvard.edu.
*E-mail: cheng.dengfeng@zs-hospital.sh.cn.
*E-mail: yanxy@sun5.ibp.ac.cn.

Author Contributions

#Y.Z. and M.L contributed equally to this work

Notes

The authors declare no competing financial interest.

ACKNOWLEDGMENTS

We thank Xiaojun Huang and Gang Ji for excellent technical support in cryo-EM imaging at the Transmission EM Facilities, Center for Biological Imaging, Institute of Biophysics. We also thank Jianping Zhang and Yingjian Zhang at the Bio Medical Imaging Research Center, Fudan University for SPECT/CT imaging. This work was supported by the following grants: National Natural Science Foundation of China (81571728, 81201698, 31530026, 81471706, 81201130 and 81271608), National Science and Technology Major Project (2013ZX10004102, 2012ZX10002-009016, 2016ZX10002014-006), Shanghai Pujiang Programme (13PJ1401400), Shanghai Municipal Commission of Health and Family Planning (XYQ2013106), 973 Program (2012CB934003), Strategic Priority Research Program of the Chinese Academy of Sciences (XDA09030306), and Youth Innovation Promotion Association CAS.

REFERENCES

(1) Yankeelov, T. E.; Abramson, R. G.; Quarles, C. C. Quantitative Multimodality Imaging in Cancer Research and Therapy. *Nat. Rev. Clin. Oncol.* **2014**, *11*, 670−680.

(2) Gambhir, S. S. Molecular Imaging of Cancer with Positron Emission Tomography. *Nat. Rev. Cancer* **2002**, *2*, 683−693.

(3) Marzola, P.; Osculati, F.; Sbarbati, A. High Field MRI in Preclinical Research. *Eur. J. Radiol.* **2003**, *48*, 165−170.

(4) Service, R. F. New Dynamic Duo: PET, MRI, Joined for the First Time. *Science* **1996**, *272*, 1423.

(5) Judenhofer, M. S.; Cherry, S. R. Applications for Preclinical PET/MRI. *Semin. Nucl. Med.* **2013**, *43*, 19−29.

(6) Bouziotis, P.; Psimadas, D.; Tsotakos, T.; Stamopoulos, D.; Tsoukalas, C. Radiolabeled Iron Oxide Nanoparticles as Dual-Modality SPECT/MRI and PET/MRI Agents. *Curr. Top. Med. Chem.* **2012**, *12*, 2694−2702.

(7) Frangioni, J. V. New Technologies for Human Cancer Imaging. *J. Clin. Oncol.* **2008**, *26*, 4012−4021.

(8) Shapiro, E. M.; Skrtic, S.; Sharer, K.; Hill, J. M.; Dunbar, C. E.; Koretsky, A. P. MRI Detection of Single Particles for Cellular Imaging. *Proc. Natl. Acad. Sci. U. S. A.* **2004**, *101*, 10901−10906.

(9) de Rosales, R. T. Potential Clinical Applications of Bimodal PET-MRI or SPECT-MRI Agents. *J. Labelled Compd. Radiopharm.* **2014**, *57*, 298−303.

(10) Relling, M. V.; Dervieux, T. Pharmacogenetics and Cancer Therapy. *Nat. Rev. Cancer* **2001**, *1*, 99−108.

(11) Ford, G. C.; Harrison, P. M.; Rice, D. W.; Smith, J. M.; Treffry, A.; White, J. L.; Yariv, J. Ferritin: Design and Formation of an Iron-Storage Molecule. *Philos. Trans. R. Soc., B* **1984**, *304*, 551−565.

(12) Theil, E. C. Ferritin: Structure, Gene Regulation, and Cellular Function in Animals, Plants, and Microorganisms. *Annu. Rev. Biochem.* **1987**, *56*, 289−315.

(13) Meldrum, F. C.; Heywood, B. R.; Mann, S. Magnetoferritin: In vitro Synthesis of a Novel Magnetic Protein. *Science* **1992**, *257*, 522−523.

(14) Klem, M. T.; Mosolf, J.; Young, M.; Douglas, T. Photochemical Mineralization of Europium, Titanium, and Iron Oxyhydroxide Nanoparticles in the Ferritin Proteincage. *Inorg. Chem.* **2008**, *47*, 2237−2239.

(15) Wong, K. K. W.; Mann, S. Biomimetic Synthesis of Cadmium Sulfide Ferritin Nanocomposites. *Adv. Mater.* **1996**, *8*, 928−932.

(16) Li, L.; Fang, C. J.; Ryan, J. C.; Niemi, E. C.; Lebrón, J. A.; Björkman, P. J.; Arase, H.; Torti, F. M.; Torti, S. V.; Nakamura, M. C.; Seaman, W. E. Binding and Uptake of H-ferritin are Mediated by Human Transferrin Receptor-1. *Proc. Natl. Acad. Sci. U. S. A.* **2010**, *107*, 3505−3510.

(17) Zhen, Z.; Tang, W.; Chen, H.; Lin, X.; Todd, T.; Wang, G.; Cowger, T.; Chen, X.; Xie, J. RGD-Modified Apoferritin Nanoparticles for Efficient Drug Delivery to Tumors. *ACS Nano* **2013**, *7*, 4830−4837.

(18) Uchida, M.; Flenniken, M. L.; Allen, M.; Willits, D. A.; Crowley, B. E.; Brumfield, S.; Willis, A. F.; Jackiw, L.; Jutila, M.; Young, M. J.; Douglas, T. Targeting of Cancer Cells with Ferrimagnetic Ferritin Cage Nanoparticles. *J. Am. Chem. Soc.* **2006**, *128*, 16626−16633.

(19) Lin, X.; Xie, J.; Niu, G.; Zhang, F.; Gao, H.; Yang, M.; Quan, Q.; Aronova, M. A.; Zhang, G.; Lee, S.; Leapman, R.; Chen, X. Chimeric Ferritin Nanocages for Multiple Function Loading and Multimodal Imaging. *Nano Lett.* **2011**, *11*, 814−819.

(20) Zhen, Z.; Tang, W.; Guo, C.; Chen, H.; Lin, X.; Liu, G.; Fei, B.; Chen, X.; Xu, B.; Xie, J. Ferritin Nanocages to Encapsulate and Deliver Photosensitizers for Efficient Photodynamic Therapy Against Cancer. *ACS Nano* **2013**, *7*, 6988−6996.

(21) Falvo, E.; Tremante, E.; Fraioli, R.; Leonetti, C.; Zamparelli, C.; Boffi, A.; Morea, V.; Ceci, P.; Giacomini, P. Antibody-Drug Conjugates: Targeting Melanoma with Cisplatin Encapsulated in Protein-Cage Nanoparticles Based on Human Ferritin. *Nanoscale* **2013**, *5*, 12278−12285.

(22) Fan, K.; Cao, C.; Pan, Y.; Lu, D.; Yang, D.; Feng, J.; Song, L.; Liang, M.; Yan, X. Magnetoferritin Nanoparticles for Targeting and Visualizing Tumour Tissues. *Nat. Nanotechnol.* **2012**, *7*, 459−464.

(23) Liang, M.; Fan, K.; Zhou, M.; Duan, D.; Zheng, J.; Yang, D.; Feng, J.; Yan, X. H-Ferritin−Nanocaged Doxorubicin Nanoparticles specifically Target and Kill Tumors with a Single-Dose Injection. *Proc. Natl. Acad. Sci. U. S. A.* **2014**, *111*, 14900−14905.

(24) Hopkins, C. R. Intracellular Routing of Transferrin and Transferrin Receptors in Epidermoid Carcinoma A431 Cells. *Cell* **1983**, *35*, 321−330.

(25) Dautry-Varsat, A.; Ciechanover, A.; Lodish, H. F. pH and The Recycling of Transferrin during Receptor-Mediated Endocytosis. *Proc. Natl. Acad. Sci. U. S. A.* **1983**, *80*, 2258−2262.

(26) Thomas, R.; Park, I. K.; Jeong, Y. Y. Magnetic Iron Oxide Nanoparticles for Multimodal Imaging and Therapy of Cancer. *Int. J. Mol. Sci.* **2013**, *14*, 15910−15930.

(27) Liu, S.; Jia, B.; Qiao, R.; Yang, Z.; Yu, Z.; Liu, Z.; Liu, K.; Shi, J.; Ouyang, H.; Wang, F.; Gao, M. A Novel Type of Dual-Modality Molecular Probe for MR and Nuclear Imaging of Tumor: Preparation, Characterization and in vivo Application. *Mol. Pharmaceutics* **2009**, *6*, 1074−1082.

(28) Lee, H. Y.; Li, Z. B.; Chen, K.; Hsu, A. R.; Xu, C.; Xie, J.; Sun, S.; Chen, X. PET/MRI Dual-Modality Tumor Imaging Using Arginine-Glycine-Aspartic (RGD)−Conjugated Radiolabeled Iron Oxide Nanoparticles. *J. Nucl. Med.* **2008**, *49*, 1371−1379.

(29) Xue, S.; Zhang, C.; Yang, Y.; Zhang, L.; Cheng, D.; Zhang, J.; Shi, H.; Zhang, Y. ^{99m}Tc-Labeled Iron Oxide Nanoparticles for Dual-Contrast (T1/T2) Magnetic Resonance and Dual-Modality Imaging of Tumor Angiogenesis. *J. Biomed. Nanotechnol.* **2015**, *11*, 1027−1037.

(30) Xie, J.; Chen, K.; Huang, J.; Lee, S.; Wang, J.; Gao, J.; Li, X.; Chen, X. PET/NIRF/MRI Triple Functional Iron Oxide Nanoparticles. *Biomaterials* **2010**, *31*, 3016−3022.

(31) Poulin, E.; Lebel, R.; Croteau, E.; Blanchette, M.; Tremblay, L.; Lecomte, R.; Bentourkia, M.; Lepage, M. Conversion of Arterial Input Functions for Dual Pharmacokinetic Modeling Using Gd-DTPA/MRI and ^{18}F-FDG/PET. *Magn. Reson. Med.* **2013**, *69*, 781−792.

(32) Choi, J. S.; Park, J. C.; Nah, H.; Woo, S.; Oh, J.; Kim, K. M.; Cheon, G. J.; Chang, Y.; Yoo, J.; Cheon, J. A. Hybrid Nanoparticle Probe for Dual-Modality Positron Emission Tomography and

DOI: 10.1021/acsnano.5b07408
ACS Nano 2016, 10, 4184−4191

Magnetic Resonance Imaging. *Angew. Chem., Int. Ed.* **2008**, *47*, 6259−6262.
(33) Madru, R.; Kjellman, P.; Olsson, F.; Wingårdh, K.; Ingvar, C.; Ståhlberg, F.; Olsrud, J.; Lätt, J.; Fredriksson, S.; Knutsson, S.; Strand, S. E. ^{99m}Tc-Labeled Superparamagnetic Iron Oxide Nanoparticles for Multimodality SPECT/MRI of Sentinel Lymph Nodes. *J. Nucl. Med.* **2012**, *53*, 459−463.
(34) Torres Martin de Rosales, R.; Tavaré, R.; Glaria, A.; Varma, G.; Protti, A.; Blower, P. J. ^{99m}Tc-Bisphosphonate-Iron Oxide Nanoparticle Conjugates for Dual-Modality Biomedical Imaging. *Bioconjugate Chem.* **2011**, *22*, 455−465.
(35) Luo, J.; Wilson, J. D.; Zhang, J.; Hirsch, J. I.; Dorn, H. C.; Fatouros, P. P.; Shultz, M. D. A Dual PET/MR Imaging Nanoprobe: ^{124}I Labeled Gd_3N@C80. *Appl. Sci.* **2012**, *2*, 465−478.
(36) Kumar, A.; Zhang, S.; Hao, G.; Hassan, G.; Ramezani, S.; Sagiyama, K.; Lo, S. T.; Takahashi, M.; Sherry, A. D.; Öz, O. K.; Kovacs, Z.; Sun, X. Molecular Platform for Design and Synthesis of Targeted Dual-Modality Imaging Probes. *Bioconjugate Chem.* **2015**, *26*, 549−558.
(37) Rohrer, M.; Bauer, H.; Mintorovitch, J.; Requardt, M.; Weinmann, H. J. Comparison of magnetic properties of MRI contrast media solutions at different magnetic field strengths. *Invest. Radiol.* **2005**, *40*, 715−724.
(38) Lee, N.; Hyeon, T. Designed Synthesis of Uniformly Sized Iron Oxide Nanoparticles for Efficient Magnetic Resonance Imaging Contrast Agents. *Chem. Soc. Rev.* **2012**, *41*, 2575−2589.
(39) Cao, C. Q.; Tian, L. X.; Liu, Q. S.; Liu, W. F.; Chen, G. J.; Pan, Y. X. Magnetic Characterization of Noninteracting, Randomly Oriented, Nanometer-Scale Ferrimagnetic Particles. *J. Geophys. Res.* **2010**, *115*, B07103.
(40) Mann, S.; Bannister, J. V.; Williams, R. J. Structure and Composition of Ferritin Cores Isolated from Human Spleen, Limpet (Patella vulgata) Hemolymph and Bacterial (Pseudomonas Aeruginosa) Cells. *J. Mol. Biol.* **1986**, *188*, 225−232.
(41) Chen, F.; Hong, H.; Goel, S.; Graves, S. A.; Orbay, H.; Ehlerding, E. B.; Shi, S.; Theuer, C. P.; Nickles, R. J.; Cai, W. *In vivo* Tumor Vasculature Targeting of CuS@ MSN Based Theranostic Nanomedicine. *ACS Nano* **2015**, *9*, 3926−3934.
(42) Song, I. H.; Lee, T. S.; Park, J. H.; Kim, K. I.; Lee, Y. J.; Kang, J. H.; woon Choi, C.; Lim, S. M. Immuno-PET Imaging and Radioimmunotherapy of ^{64}Cu/^{177}Lu Labeled anti-EGFR Antibody in Esophageal Squamous Cell Carcinoma. *J. Nucl. Med.* **2015**, *56*, 1216−1216.
(43) Hainfeld, J. F. Uranium-Loaded Apoferritin with Antibodies Attached: Molecular Design for Uranium Neutron-Capture Therapy. *Proc. Natl. Acad. Sci. U. S. A.* **1992**, *89*, 11064−11068.
(44) Aime, S.; Frullano, L.; Geninatti Crich, S. Compartmentalization of a Gadolinium Complex in the Apoferritin Cavity: a Route to Obtain High Relaxivity Contrast Agents for Magnetic Resonance Imaging. *Angew. Chem., Int. Ed.* **2002**, *41*, 1017−1019.
(45) Geninatti Crich, S.; Bussolati, B.; Tei, L.; Grange, C.; Esposito, G.; Lanzardo, S.; Camussi, G.; Aime, S. Magnetic Resonance Visualization of Tumor Angiogenesis by Targeting Neural Cell Adhesion Molecules with the Highly Sensitive Gadolinium-Loaded Apoferritin Probe. *Cancer Res.* **2006**, *66*, 9196−9201.
(46) Domínguez-Vera, J. M. Iron(III) Complexation of Desferrioxamine B Encapsulated in Apoferritin. *J. Inorg. Biochem.* **2004**, *98*, 469−472.
(47) Cutrin, J. C.; Crich, S. G.; Burghelea, D.; Dastrù, W.; Aime, S. Curcumin/Gd Loaded Apoferritin: A Novel "Theranostic" Agent to Prevent Hepatocellular Damage in Toxic Induced Acute Hepatitis. *Mol. Pharmaceutics* **2013**, *10*, 2079−2085.
(48) Jeon, J. O.; Kim, S.; Choi, E.; Shin, K.; Cha, K.; So, I. S.; Kim, S. J.; Jun, E.; Kim, D.; Ahn, H. J.; Lee, B. H.; Lee, S. H.; Kim, I. S. Designed Nanocage Displaying Ligand-Specific Peptide Bunches for High Affinity and Biological Activity. *ACS Nano* **2013**, *7*, 7462−7471.
(49) Li, X.; Qiu, L.; Zhu, P.; Tao, X.; Imanaka, T.; Zhao, J.; Huang, Y.; Tu, Y.; Cao, X. Epidermal Growth Factor-Ferritin H-Chain Protein Nanoparticles for Tumor Active Targeting. *Small* **2012**, *8*, 2505−2514.
(50) Visser, G. W.; Klok, R. P.; Gebbinck, J. W.; ter Linden, T.; van Dongen, G. A.; Molthoff, C. F. Optimal Quality ^{131}I-monoclonalantibodies on High-Dose Labeling in a Large Reaction Volume and Temporarily Coating the Antibody with IODO-GEN. *J. Nucl. Med.* **2001**, *42*, 509−519.

DOI: 10.1021/acsnano.5b07408
ACS Nano 2016, 10, 4184−4191